Position and Speed Detection Method Based on Cross-Decoupling Network Filtering for Gearless Traction Motor Drives at Low-Speed Operation

Yin Bai, Gaolin Wang, *Senior Member, IEEE*, Guoqiang Zhang, *Member, IEEE*, Nannan Zhao, *Member, IEEE*, and Dianguo Xu, *Fellow, IEEE*

***Abstract*—This article proposes a position and speed detection method based on the cross-decoupling network filtering (CDNF) method combined with phase-locked loop (PLL). This method is used to enhance the detection precision of position and reduce the speed fluctuations at low-speed operation for gearless traction motor drives with an ordinary-resolution encoder. The harmonic distributions of the discontinuous orthogonal position signal in low-speed region are analyzed. On this basis, the position and speed detection method based on CDNF with PLL is presented to obtain the harmonics of the discontinuous position signal adaptively for eliminating the position detection error and improving the accuracy of the speed feedback. The criteria of the filter parameter design are presented based on the maximum phase margin theory to maintain the stability of the system. Experiments were carried out on an 11.7 kW permanent magnet gearless traction motor drive with an ordinary-resolution encoder installed. The experimental results verify the effectiveness of the proposed method at low-speed operation.**

***Index Terms*—Discontinuous position, gearless traction motor drives, low-speed operation, ordinary-resolution encoder, phase-locked loop.**

I. Introduction

PERMANENT magnet synchronous motors (PMSMs) have been widely used in industrial applications due to the high efficiency, good performance, and high-power density [1]–[4]. In the gearless elevator traction system, PMSM is mainly used as the traction motor to improve performance, save energy, and reduce space. The rotor position needs to be detected through an encoder to obtain the accurate position and speed signals for the field-oriented control. Nowadays, high-resolution encoders are difficult to meet the cost-effective development of gearless traction system. When the elevator motor drives use relatively cheap ordinary-resolution encoders, the speed fluctuations caused by the discontinuous position signal behave obvious at low-speed operation. The fluctuations would decrease the riding comfort of the elevator. Therefore, it is a challenge to obtain accurate rotor position and speed information for gearless traction motor drive system installed with an ordinary-resolution encoder.

At present, a lot of research works have been carried out to investigate this issue. The literatures are mainly divided into model-based and nonmodel-based methods. The model-based method needs to detect the rotor position through the motor model and the parameters, such as Luenberger observer, sliding mode observer, etc. [5]–[12]. The mechanical equation of PMSM is always used to ensure the estimated position converge to the actual one. Careful selection of the observer bandwidth is needed to ensure accurate estimation of the position and speed. A sliding mode control method combined with extended state observer (ESO) was presented to estimate the position and speed [5]. In this method, ESO was used to observe the lumped disturbance, which could obtain less observation error of position. A cascade observer was proposed to reduce the speed detection error in [6]. This observer used a second-order sliding mode controller to get the rotor position accurately. It needs to consider the system convergence carefully when using combination of two kinds of observers, which would increase the order of the system.

In order to improve the bandwidth of the position and speed observers, the adaptive law can be applied in model-based method. The observers can adjust the response by adaptive law, which will help to improve the dynamic performance of the system [7]–[9]. A sliding mode observer using the adaptive law based on the least square method was proposed to suppress the harmonics generated by the nonlinear characteristics of inverter [7]. Meanwhile the adaptive law based on the frequency tracking controller was used to track the back-EMF of the motor according to the variation of operating frequency [8]. The model-based method can observe the rotor position on the premise that the motor parameters are known exactly [9]. If the motor parameters are inaccurate, the high-precision rotor position is difficult to obtain.

The nonmodel-based method is mainly divided into interpolation method and filtering method. For the interpolation method, the detection of position signal mainly depends on the selection of appropriate interpolation basis functions to predict the position of the next sampling period [10]–[20]. The precision

Manuscript received July 20, 2020; revised November 7, 2020 and January 16, 2021; accepted March 14, 2021. Date of publication March 22, 2021; date of current version June 30, 2021. This work was supported by the Research Fund for the National Natural Science Foundation of China under Grants 51961130385 and 52007039. Recommended for publication by Associate Editor T. Shi. *(Corresponding author: Gaolin Wang.)*

The authors are with the School of Electrical Engineering and Automation, Harbin Institute of Technology, Harbin 150001, China (e-mail: 2205366869@qq.com; wgl818@hit.edu.cn; zhgq@hit.edu.cn; 15104691306@126.com; xudiang@hit.edu.cn).

Color versions of one or more figures in this article are available at https://doi.org/10.1109/TPEL.2021.3067674.

Digital Object Identifier 10.1109/TPEL.2021.3067674

of the position signal after fitting is determined by the carrier frequency of the control system. In general, the precision is higher than that of the position signal obtained by the encoder [12]–[14], [16]. Therefore, the speed acquired by differential fitting position signal has fewer fluctuations. The fitting precision of the position is related to the selection of the interpolation basis function [20]. Improper selection of interpolation basis function or parameters will lead to inaccurate fitting and even instability of the system. The radial basis function was set to update the basis function for tracking the position effectively [15]. A moving least square (MLS) algorithm was used to obtain the high-precision estimation of discrete positions [18]. The interpolation method tends to produce noise in rotor position, and it will cause the phase delay of the estimated position.

Another nonmodel-based method is the filtering method, which can obtain continuous position by dealing with the original discrete position signals. With the development of digital control system, filtering schemes are convenient to be used in the rotor position estimation. It can effectively extract the harmonics in the back-EMF signal [21]–[25]. A least square adaptive filter was used to obtain the harmonics of the back-EMF, which can realize the frequency adaption [21]. A proportional resonant (PR) controller under low carrier radio was proposed to get the harmonics in original position signal [22]. The existing filtering method can estimate the rotor position and the speed using the lower-bits encoder such as Hall sensors. Once the resolution of the encoder increases, the harmonic frequencies in the rotor position become higher [25]. These methods have the common way of constructing harmonics, which could get distorted if the frequency of the harmonics is close to the PWM frequency of the system. Hence, it still needs further study in the filtering methods to improve the precision of position using the ordinary-resolution encoder in low-speed operation.

This article proposes a detection method based on the cross-decoupling network filtering (CDNF) method combined with phase-locked loop (PLL) to detect the rotor position and speed of gearless traction motor using an ordinary-resolution encoder. Based on the analysis of harmonics in orthogonal signal of position, the CDNF method is constructed to eliminate the harmonics in the discontinuous orthogonal signal. Then, the accurate position signal can be extracted through PLL. In order to further simplify the complexity of CDNF, the harmonics of adjacent frequencies are combined to reduce the number of subharmonic filters, which can achieve the satisfactory performance. Furthermore, the selection criteria of parameters are given to maintain the stability of the system. The effectiveness of the scheme is verified on 11.7 kW gearless traction motor drive test platform.

II. Harmonic Analysis of Position Signal for Gearless Elevator Motor Drives at Low Speed

The field-oriented control scheme for gearless traction motor drive system is shown in Fig. 1. The PMSM is used as a traction motor in the elevator, and an ordinary-resolution encoder is used as rotor position sensor, which is the incremental encoder. When the traction motor works at low speed, there exists the problem

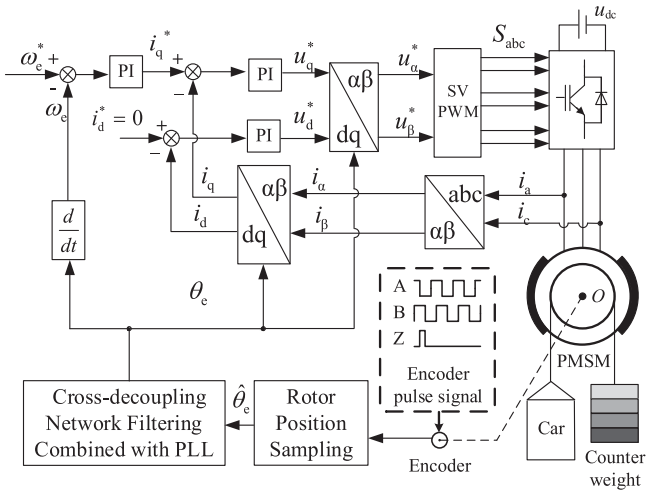

Fig. 1. Block diagram of field-oriented control system for gearless traction motor drive.

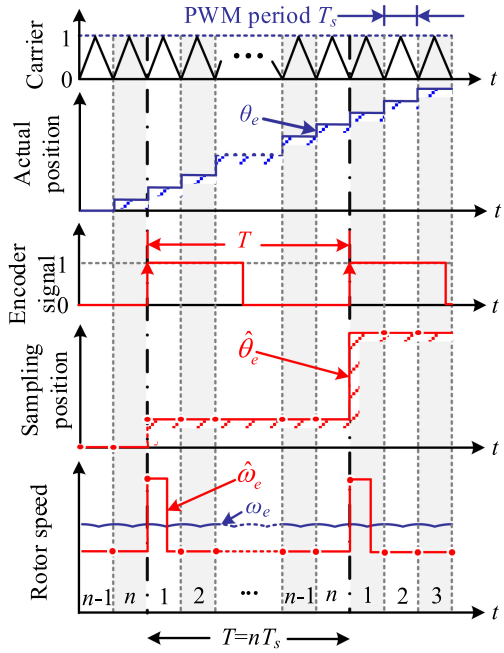

Fig. 2 Analysis of low-precision rotor position and speed fluctuations at low speed using ordinary-resolution encoder.

of low-sampling ratio of rotor position, which would decrease the riding comfort of the elevator.

The analysis of the original rotor position and speed information obtained by the digital control system using an ordinary-resolution encoder at low-speed operation are shown in Fig. 2. In Fig. 2, T is defined as the time interval between the two sampling pulses of the encoder, and the carrier period of the field-oriented control system of the traction motor is T_s. The relationship between T and T_s satisfies $T = nT_s$. When $n \leq 1$ and $T \leq T_s$, the count value of the encoder can be updated within each PWM carrier period. When $n > 1$ and $T > T_s$, it cannot ensure that the count value of the encoder can be updated within each PWM carrier period. However, only within n PWM carrier periods can the count value of the encoder be updated once. The speed

obtained by differentiating the position signal contains obvious fluctuation. This kind of speed ripple affects the comfort of passengers. In general, *T* method has been commonly used for speed detection in the low-speed region. However, in extremely low-speed region, only one encoder pulse can be sampled within multiple cycles of the speed loop. When the speed changes, the calculated speed is updated only after several speed loop cycles, which may behave large speed error. Besides, long time interval for updating the speed due to the low-encoder resolution may cause a large delay in the speed calculated by *T* method. Hence, more accurate position and speed detection algorithms need to be studied.

In order to analyze the harmonic distributions of the detected position and speed at low-speed operation, the sampling position signal from the encoder in Fig. 1 is orthogonalized in the stationary $\alpha\beta$-axes coordinate system

$$\begin{cases} \boldsymbol{H}(\alpha) = \cos(\hat{\theta}_e) \\ \boldsymbol{H}(\beta) = \sin(\hat{\theta}_e) \end{cases} \tag{1}$$

where $\hat{\theta}_e$ is the discontinuous rotor position signal obtained from the encoder. $\boldsymbol{H}(\alpha)$ and $\boldsymbol{H}(\beta)$ are a pair of orthogonal scalar signals. The position information can be expressed as a rotating space vector signal. $\boldsymbol{H}(\alpha)$ and $\boldsymbol{H}(\beta)$ can be expressed as

$$\boldsymbol{H} = \boldsymbol{H}(\alpha) + j\boldsymbol{H}(\beta). \tag{2}$$

The real part and the imaginary part of the orthogonal signal are both expressed by Fourier series, which can be obtained as

$$\begin{cases} \boldsymbol{H}(\alpha) = \sum_{k=1}^{\infty} \alpha_k \cos(k\theta_e) \\ \boldsymbol{H}(\beta) = \sum_{k=1}^{\infty} \beta_k \sin(k\theta_e) \end{cases} \tag{3}$$

where θ_e is the continuous rotor position, k is an integer number with the range of $[1, +\infty)$, α_k and β_k are the coefficients of the Fourier series, which can be expressed as

$$\alpha_k = \begin{cases} 0, & k \neq p*N+1 \\ \cos(\frac{\pi}{kN}), k = p*N+1 \end{cases} \quad p = 1, 2, 3 \ldots \tag{4a}$$

$$\beta_k = \begin{cases} 0, & k \neq p*N+1 \\ sin(\frac{\pi}{kN}), k = p*N+1 \end{cases} \quad p = 1, 2, 3 \ldots \tag{4b}$$

where *N* represents the resolution of the encoder, and *p* is a positive integer. The harmonic distribution of discrete orthogonal position signals can be obtained through (3). Further, $\boldsymbol{H}(\alpha)$ and $\boldsymbol{H}(\beta)$ can be expressed as

$$\begin{cases} \boldsymbol{H}(\alpha) = \cos(\theta_e - \psi) + \sum\limits_{k=1}^{\infty} [\frac{1}{1-kN} cos(k\omega_i t - \theta_e + \psi)] \\ \qquad\qquad + \sum\limits_{k=1}^{\infty} [\frac{1}{kN+1} cos(k\omega_i t + \theta_e - \psi)] \\ \boldsymbol{H}(\beta) = \sin(\theta_e - \psi) + \sum\limits_{k=1}^{\infty} [\frac{1}{kN-1} sin(k\omega_i t - \theta_e + \psi)] \\ \qquad\qquad + \sum\limits_{k=1}^{\infty} [\frac{1}{kN+1} sin(k\omega_i t + \theta_e - \psi)] \end{cases} \tag{5}$$

where ω_i is the harmonic frequency of the discontinuous position signal, satisfying $\omega_i t = N\theta_e$, and ψ is the phase error, satisfying $\psi = \pi/N$.

The relationship between the corresponding fundamental and harmonic components of spatial rotation vector in $\alpha\beta$-axes is shown in Fig. 3. In the space vector coordinate system, $\boldsymbol{H}$ is the position space rotating vector calculated by $\hat{\theta}_e$. The trajectory of

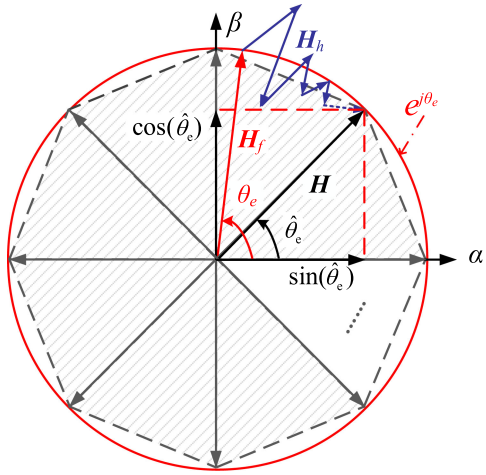

Fig. 3. Spatial rotation vector of the orthogonal position signals with harmonic distribution.

$\boldsymbol{H}$ is a positive *N*-sided shape, since $\hat{\theta}_e$ varies discretely. $\boldsymbol{H}$ can be divided into the fundamental component $\boldsymbol{H}_f$ and the harmonic component $\boldsymbol{H}_h$. Then, $\boldsymbol{H}$, $\boldsymbol{H}_f$, and $\boldsymbol{H}_h$ satisfy

$$\begin{aligned} \boldsymbol{H} &= \boldsymbol{H}_f + \boldsymbol{H}_h \\ &= e^{j(\hat{\theta}_e - \psi)} + \sum_{k=1}^{\infty} \\ &\left[-\frac{1}{kN-1} e^{-j(k\omega_i t - \hat{\theta}_e + \psi)} + \frac{1}{kN+1} e^{j(k\omega_i t + \hat{\theta}_e - \psi)} \right]. \end{aligned} \tag{6}$$

From (6), it can be seen that $\boldsymbol{H}_f$ is constituted by continuous rotor position vector θ_e, whose trajectory is the circumscribed circle of the trajectory of $\boldsymbol{H}$. Meanwhile the harmonic component $\boldsymbol{H}_h$ results in discontinuous motion of $\boldsymbol{H}$. Therefore, $\boldsymbol{H}_h$ needs to be filtered out to obtain accurate rotor position.

III. Position and Speed Detection Method Based on CDNF With PLL

A. Strategy of Position and Speed Detection

The position and speed detection method of gearless traction motor drive system based on CDNF with PLL is shown in Fig. 4.

The orthogonal pulse information output by the encoder is calculated to obtain the discontinuous rotor position of the traction motor. First, a group of discontinuous orthogonal signals can be obtained after the orthogonalization of sampled position signal, which is used as the input of cross-decoupling network filter. The output signals become a group of continuous orthogonal signals after digital filtering, which contains accurate rotor position information. Then, PLL is adopted to extract the position and the speed information.

B. CDNF of Orthogonal Position Signal

The block diagram of the CDNF method for attenuating position error is shown in Fig. 5. In CDNF, the discrete orthogonal position signals are taken as the input. The fundamental

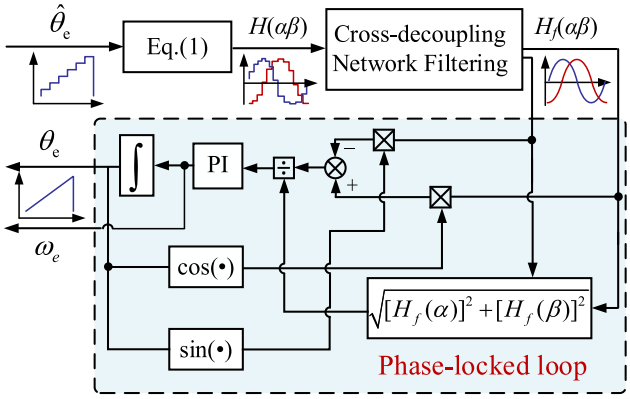

Fig. 4. Block diagram of position and speed detection method based on CDNF with PLL.

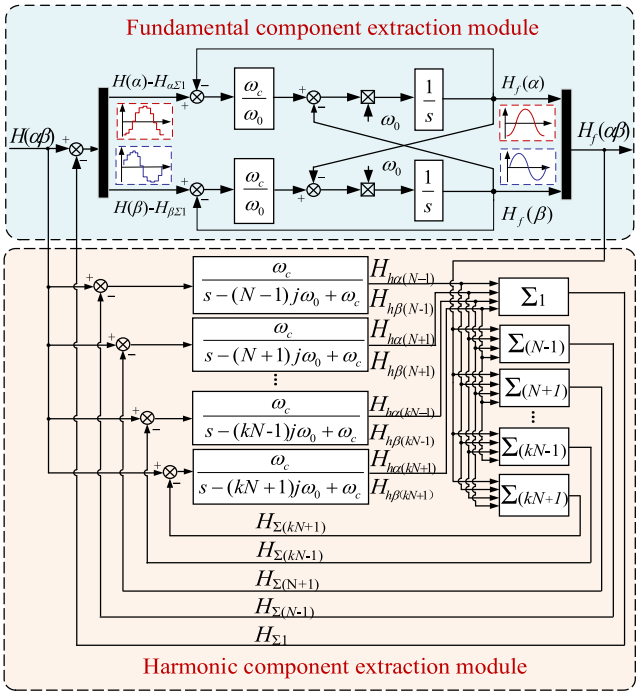

Fig. 5. Block diagram of CDNF to extract rotor position information.

component and each harmonic can be extracted and the remaining harmonics are subtracted from the input. Only the current harmonic part of the input is retained. In this scheme, CDNF forms harmonic feedback loops, which will filter the harmonics of each order effectively.

From Fig. 5, the structure of CDNF contains two parts, the fundamental component extraction module and the harmonic component extraction module. Both two extraction modules are designed based on the complex filter. According to [27], the transfer function of the fundamental component extraction module based on complex filter can be shown as

$$\boldsymbol{F}_f(s) = \frac{\boldsymbol{H}_f(\alpha)}{\boldsymbol{H}(\alpha)} = \frac{\omega_c}{s - j\omega_0 + \omega_c} \tag{7}$$

where ω_0 is the fundamental frequency of the discontinuous orthogonal position signal, and ω_c is the cut-off frequency of complex filter. The real and imaginary parts of the fundamental

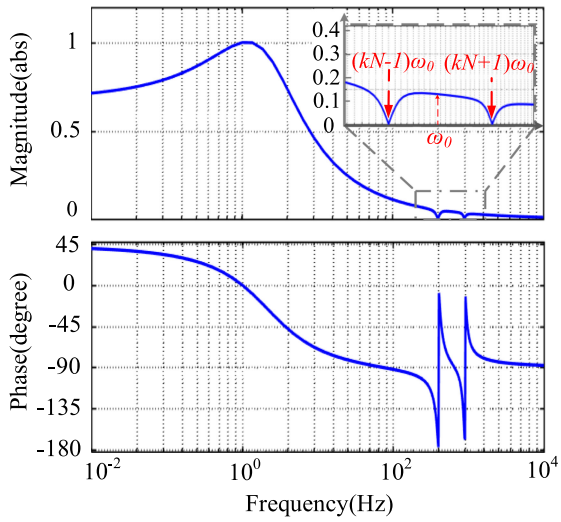

Fig. 6. Bode diagram of CDNF.

component of the spatial rotation vector can be obtained through (6)

$$\begin{bmatrix} \boldsymbol{H}_f(\alpha) \\ \boldsymbol{H}_f(\beta) \end{bmatrix} = \frac{\omega_c}{s^2 + 2\omega_c s + \omega_c^2 + \omega_0^2} \boldsymbol{H}_0 \begin{bmatrix} \boldsymbol{H}(\alpha) - \boldsymbol{H}_{\alpha\Sigma 1} \\ \boldsymbol{H}(\beta) - \boldsymbol{H}_{\beta\Sigma 1} \end{bmatrix} \tag{8a}$$

$$\boldsymbol{H}_0 = \begin{bmatrix} s + \omega_c & -\omega_0 \\ \omega_0 & s + \omega_c \end{bmatrix} \tag{8b}$$

where $\boldsymbol{H}_f(\alpha)$ and $\boldsymbol{H}_f(\beta)$ are the fundamental components in the discontinuous orthogonal position signal, $\boldsymbol{H}_{\alpha\Sigma 1}$ and $\boldsymbol{H}_{\beta\Sigma 1}$ are the components except for the other harmonic components.

The harmonic component extraction module consists of subharmonic extraction modules of different frequencies. Each subharmonic extraction module extracts only one frequency of harmonic. Suppose that ω_{kN-1} is the frequency of $(kN-1)$th harmonic, and ω_{kN+1} is the frequency of $(kN+1)$th harmonic. The frequencies between the fundamental component and the high harmonics satisfy $\omega_{kN-1} = (kN\text{-}1)\omega_0, \omega_{kN+1} = (kN+1)\omega_0$. The transfer functions between the input signal and the extracted harmonics in Fig. 8 can be expressed as

$$\begin{cases} \boldsymbol{F}_{h(kN-1)}(s) = \dfrac{\boldsymbol{H}_{h(kN-1)}(\alpha)}{\boldsymbol{H}(\alpha)} = \dfrac{\omega_c}{s-(kN-1)j\omega_0+\omega_c} \\ \boldsymbol{F}_{h(kN+1)}(s) = \dfrac{\boldsymbol{H}_{h(kN+1)}(\alpha)}{\boldsymbol{H}(\alpha)} = \dfrac{\omega_c}{s-(kN+1)j\omega_0+\omega_c}. \end{cases} \tag{9}$$

Eq. (9) can obtain the expressions of the real and the imaginary parts of $(kN-1)$th and $(kN+1)$th harmonics in the discontinuous orthogonal position signal

$$\begin{bmatrix} \boldsymbol{H}_{h(kN-1)}(\alpha) \\ \boldsymbol{H}_{h(kN-1)}(\beta) \end{bmatrix} = \frac{\omega_c \boldsymbol{H}_{kN-1}}{s^2 + 2\omega_c s + \omega_c^2 + (kN-1)^2\omega_0^2} \times \begin{bmatrix} \boldsymbol{H}(\alpha) - \boldsymbol{H}_{h\alpha(kN-1)} \\ \boldsymbol{H}(\beta) - \boldsymbol{H}_{h\beta(kN-1)} \end{bmatrix} \tag{10a}$$

$$\boldsymbol{H}_{kN-1} = \begin{bmatrix} s + \omega_c & -(kN-1)\omega_0 \\ (kN-1)\omega_0 & s + \omega_c \end{bmatrix} \tag{10b}$$

$$\begin{bmatrix} \boldsymbol{H}_{h(kN+1)}(\alpha) \\ \boldsymbol{H}_{h(kN+1)}(\beta) \end{bmatrix} = \frac{\omega_c \boldsymbol{H}_{kN+1}}{s^2 + 2\omega_c s + \omega_c^2 + (kN+1)^2\omega_0^2}$$

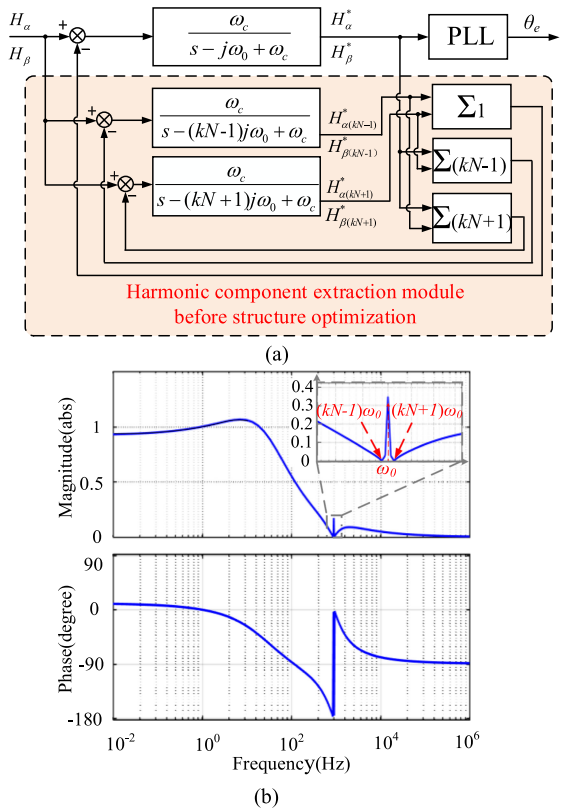

Fig. 7. Structure and Bode diagrams of CDNF without structure optimization. (a) Structure diagram. (b) Bode diagram.

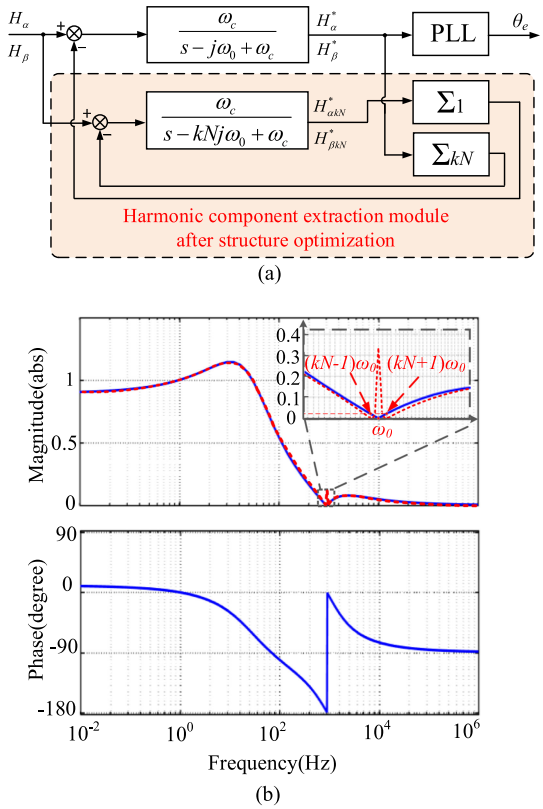

Fig. 8. Structure and Bode diagrams of CDNF with structure optimization. (a) Structure diagram (b) Bode diagram.

$$\times \begin{bmatrix} \boldsymbol{H}(\alpha) - \boldsymbol{H}_{h\alpha(kN+1)} \\ \boldsymbol{H}(\beta) - \boldsymbol{H}_{h\beta(kN+1)} \end{bmatrix} \tag{11a}$$

$$\boldsymbol{H}_{kN+1} = \begin{bmatrix} s+\omega_c & -(kN+1)\omega_0 \\ (kN+1)\omega_0 & s+\omega_c \end{bmatrix}. \tag{11b}$$

Fig. 6 shows the Bode diagram of CDNF. Taking *kN*th harmonics as an example, it can be seen that CDNF at the fundamental frequency part has the unit gain at the fundamental frequency. The gains on both sides of the fundamental frequency are rapidly attenuated, which can extract the fundamental frequency effectively. In the harmonic frequency, the absolute value of the gain drops to zero gradually, forming the notch effect, which can filter the harmonics availably. Hence CDNF can extract the continuous orthogonal position in the discrete orthogonal position, and obtain the accurate position signal combined with PLL. The traditional first-order and second-order low-pass filters are usually used to suppress the harmonic components, which perform phase delay to a variable extent. Compared with the traditional low-pass filters, the phase delay of CDNF at the fundamental frequency is 0, which can extract the fundamental frequency signal more accurately.

IV. Structure Optimization Scheme and Stability Analysis of CDNF

A. Structure Optimization Scheme of CDNF at Low Speed

In practice, the number of harmonic extraction modules should be limited to simplify the system structure. From (5), the fundamental and harmonic components of the orthogonal signal at the discontinuous position can be extracted as follows:

$$\begin{cases} \boldsymbol{H}_f(\alpha) = \cos(\theta_e - \psi) \\ \boldsymbol{H}_h(\alpha) = \sum_{k=1}^{\infty}\left[-\frac{1}{kN-1}\cos(k\omega_i t - \theta_e + \psi)\right] \\ \quad + \sum_{k=1}^{\infty}\left[\frac{1}{kN+1}\cos(k\omega_i t + \theta_e - \psi)\right] \\ \boldsymbol{H}_f(\beta) = \sin(\theta_e - \psi) \\ \boldsymbol{H}_h(\beta) = \sum_{k=1}^{\infty}\left[-\frac{1}{kN-1}\sin(k\omega_i t - \theta_e + \psi)\right] \\ \quad + \sum_{k=1}^{\infty}\left[\frac{1}{kN+1}\sin(k\omega_i t + \theta_e - \psi)\right]. \end{cases} \tag{12}$$

The harmonic components can be simplified as

$$\begin{cases} \boldsymbol{H}_h(\alpha) = \sum\limits_{k=1}^{\infty}\frac{2}{1-k^2N^2}[\cos(k\omega_i t - \theta_e + \psi) \\ \quad + \cos(k\omega_i t + \theta_e - \psi)] \\ \quad + \sum\limits_{k=1}^{\infty}\frac{2kN}{1-k^2N^2}[\cos(k\omega_i t - \theta_e + \psi) + \cos(k\omega_i t + \theta_e - \psi)] \\ \boldsymbol{H}_h(\beta) = \sum\limits_{k=1}^{\infty}\frac{2}{1-k^2N^2}[\sin(k\omega_i t - \theta_e + \psi) \\ \quad + \sin(k\omega_i t + \theta_e - \psi)] \\ \quad + \sum\limits_{k=1}^{\infty}\frac{2kN}{1-k^2N^2}[\sin(k\omega_i t - \theta_e + \psi) + \sin(k\omega_i t + \theta_e - \psi)]. \end{cases} \tag{13}$$

The ordinary-resolution encoders commonly have *N P/R* resolution while $N>>1$. So, $\frac{2}{kN-1} >> \frac{2}{k^2N^2-1}$ and

$$\begin{cases} \boldsymbol{H}_h(\alpha) \approx \sum_{k=1}^{\infty} -\frac{2kN\sin(\theta_e-\psi)}{1-k^2N^2}\cos(k\omega_i t) \\ \boldsymbol{H}_h(\beta) \approx \sum_{k=1}^{\infty} -\frac{2kN\cos(\theta_e-\psi)}{1-k^2N^2}\sin(k\omega_i t). \end{cases} \tag{14}$$

This method focuses on solving the problem of the traction motor operating at low speed in which case it can be seen that $\omega_i t \gg \theta_e$. So,$\sin(\theta_e - \psi)$ can be constant when $\sin(k\omega_i t)$

changes. Therefore, the discontinuous orthogonal position signal can be expressed as

$$\begin{cases} \boldsymbol{H}(\alpha) = \cos(\theta_e - \psi) + \sum_{k=1}^{\infty} \alpha_n \cos(k\omega_i t) \\ \boldsymbol{H}(\beta) = \sin(\theta_e - \psi) + \sum_{k=1}^{\infty} \beta_n sin(k\omega_i t) \end{cases} \tag{15}$$

where $\begin{cases} \alpha_n = \frac{2kN\sin(\theta_e-\psi)}{k^2N^2-1} \\ \beta_n = \frac{2kN\cos(\theta_e-\psi)}{k^2N^2-1} \end{cases}$.

It can be seen from the comparison between (6) and (15) that after structure optimization, the number of subharmonic extraction modules is reduced by half, which can simplify the complexity of CDNF. In the actual processing, the (*kN−1*)th and (*kN+1*)th harmonic extraction modules can be combined to filter the *kN*th harmonics directly. Moreover, the harmonics may also exist between (*kN−1*)th and (*kN+1*)th harmonics during the traction motor runs. By combining the filters, the harmonics can be attenuated between the frequencies of $(kN-1)\omega_0$ and $(kN+1)\omega_0$.

The structure and Bode diagrams of CDNF without and with the structure optimization are shown in Figs. 7 and 8, respectively. It can be seen that the harmonic extraction modules exist at the frequencies of $(kN\text{-}1)\omega_0$ and $(kN+1)\omega_0$, which acts notch at the two frequencies according to the Bode diagram in Fig. 7(b). And the absolute gain value still exists between $(kN-1)\omega_0$ and $(kN+1)\omega_0$. After the structure optimization, the harmonic extraction modules act notch at $kN\omega_0$, and the effective notch is still achieved at $(kN-1)\omega_0$ and $(kN+1)\omega_0$. The harmonics between $(kN-1)\omega_0$ and $(kN+1)\omega_0$ are still attenuated in Fig. 8(b). So, the structure optimization can simplify the structure of CDNF while maintaining the filtering effect. In fact, the harmonics at the order of $k = 1$ and $k = 2$ are the main components causing the discontinuity of position signal. So, the optimal value of k equals 1 and 2.

B. Stability Analysis of CDNF With PLL

According to the control principle, the open-loop transfer function of the system should have the maximum phase margin when the system maintains the maximum stable state. Therefore, the following analysis aims to maximize the phase margin of the system. From Fig. 4, the open-loop transfer function of the system is

$$G_{\mathrm{OL}}(s) = \frac{\{\sqrt{[\boldsymbol{H}_f(\alpha)]^2 + [\boldsymbol{H}_f(\beta)]^2}\}\omega_c(k_p s + k_i)}{\{[\boldsymbol{H}_f(\alpha)]^2 + [\boldsymbol{H}_f(\beta)]^2\}s^3 + s^2\omega_c[\boldsymbol{H}_f(\alpha)]^2 + s^2\omega_c[\boldsymbol{H}_f(\beta)]^2} \tag{16}$$

where k_p and k_i are the proportional and the integral coefficients of the PI controller, respectively. The phase margin of the system calculated by (16) can be expressed as

$$\mathrm{PM} = \arctan\left(\frac{\omega_x k_p}{k_i}\right) - \arctan\left(\frac{\omega_x}{\omega_c}\right) \tag{17}$$

where ω_x is the cross-over frequency of the system, which satisfies the following relation:

$$\omega_x \sin\left(\arctan\left(\frac{\omega_x k_p}{k_i}\right)\right) = k_p \cos\left(\arctan\left(\frac{\omega_x}{\omega_c}\right)\right). \tag{18}$$

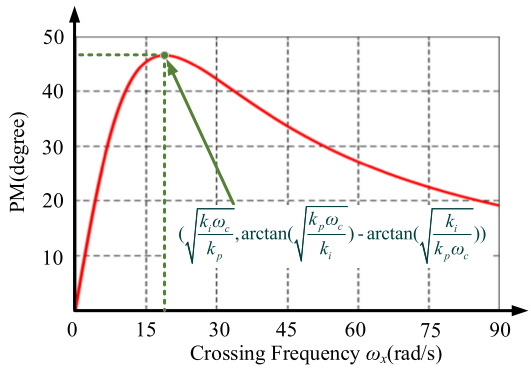

Fig. 9. Function image of phase margin on the cross-over frequency.

Fig. 9 shows the function image of the phase margin at the cross-over frequency. It can be noted that there is a maximum of the phase margin, at which the partial derivative of the phase margin with respect to the cross-over frequency is zero. The cross-over frequency and the maximum phase margin can be obtained when the phase margin is the maximum.

$$\omega_{x\max} = \sqrt{\frac{k_i\omega_c}{k_p}}, \tag{19}$$

$$\mathrm{PM}_{\max} = \arctan\left(\sqrt{\frac{k_p\omega_c}{k_i}}\right) - \arctan\left(\sqrt{\frac{k_i}{k_p\omega_c}}\right). \tag{20}$$

Substitute (19) into the expression of traversal frequency to obtain $\omega_x = k_p$. It can be seen that the proportional coefficient k_p of PLL determines the phase margin of the system. The system may have the maximum phase margin when $\omega_x = k_p$. Here, k_p, k_i and ω_c satisfy ${k_p}^3 = k_i\omega_c$. Suppose $\omega_c = m^2 k_i/k_p$, where m is constant. It can be obtained that

$$\begin{cases} k_i = \frac{{k_p}^2}{\{\sqrt{[\boldsymbol{H}_f(\alpha)]^2 + [\boldsymbol{H}_f(\beta)]^2}\}m} \\ \omega_c = \frac{m * k_p}{\{\sqrt{[\boldsymbol{H}_f(\alpha)]^2 + [\boldsymbol{H}_f(\beta)]^2}\}}. \end{cases} \tag{21}$$

The system can reach the maximum phase margin if (20) is satisfied. The phase margin is expressed by constant m

$$\mathrm{PM} = arctan\frac{m^2 - 1}{2m}. \tag{22}$$

Therefore, the phase margin of the system can be determined by the value of m. The Bode diagram of the open-loop transfer function of the system when m takes different values are shown in Fig. 10 . As can be seen from the figure, when m increases, the phase margin of the system increases gradually. The maximum of the phase margin is obtained at $\omega_x = k_p$, verifying the theory analysis.

IV. Experimental Results

The proposed position and speed detection method based on CDNF with PLL was verified on the platform of gearless traction motor system, as shown in Fig. 13. The parameters of the PMSM traction motor are shown in Table I. The whole field-oriented control algorithm is executed with a low-cost ARM chip STM32F103VB in the gearless traction motor drive

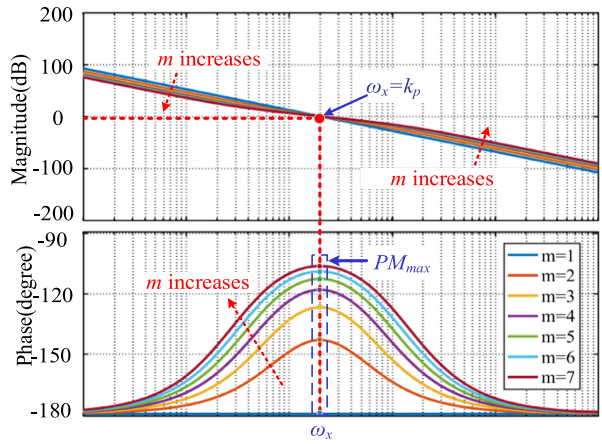

Fig. 10. Bode diagram of the open-loop transfer function of the system.

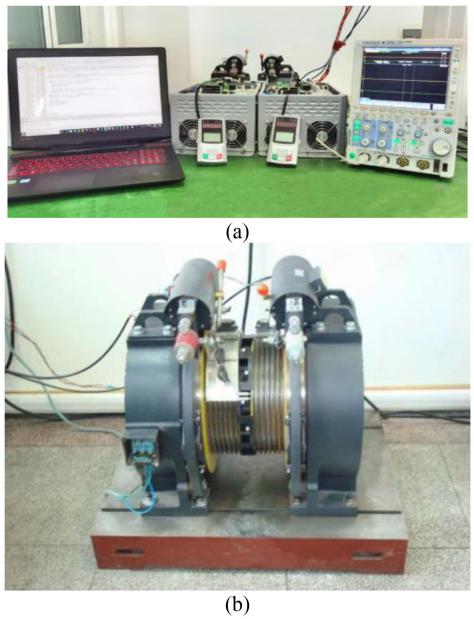

Fig. 11. Experimental platform of 11.7 kW gearless traction motor. (a) Traction motor drives. (b) Traction motor platform.

TABLE I
PMSM PARAMETERS

Parameter	Value	Parameter	Value
Rated Power	11.7kW	Rated Torque	670N·m
Rated Speed	167r/min	Resistance	0.23Ω
Rated Frequency	33.4Hz	Number of Pole Pairs	12
Rated Voltage	380V	*d*-axis Inductance	15mH
Rated Current	23A	*q*-axis Inductance	15mH

platform. The position sensor adopts ERN-1387 SIN/COS encoder whose resolution is 2048 *P*/*R*. This encoder can output both high-precision position signals and low-precision discrete position signals. In this article, the actual speed is obtained by position subdivision of SIN/COS signals from the encoder. The low-precision discrete position signal is used as the position signal to be processed, while the actual position and actual speed are used to make experimental comparison. Define the

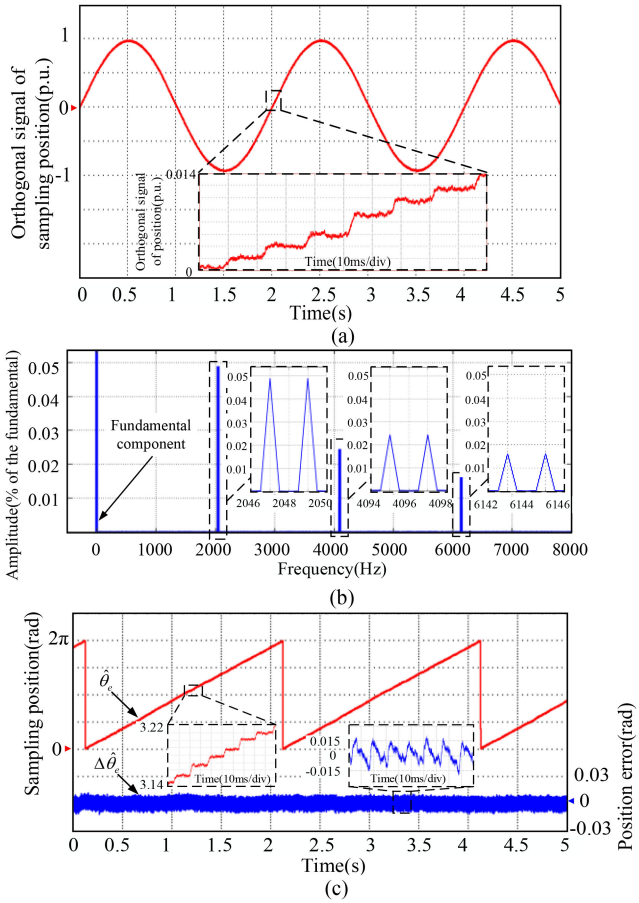

Fig. 12. Experimental results using the *M* method. (a)Discontinuous orthogonal position signal. (b) Fourier analysis of the orthogonal position signal. (c) Sampling position and position error.

position error as the difference between the actual position and the position by different method, and the speed error as the difference between the actual speed and the speed by different method. The switching frequency of inverter is set as 6 kHz. The periods of current and speed loops are set as 166.7μs and 1ms, respectively.

In this article, the least-square interpolation method [9] and *T* method are adopted to compare the effect of the proposed method. Define the sampling position is $\hat{\theta}_e$, the interpolation position is θ_i, the estimated position is θ_e. The speed obtained by the *M* method is defined as "speed by *M* method" and expressed as ω_m, the speed obtained by the traditional interpolation method is defined as "speed by interpolation" and expressed as ω_i, the speed obtained by *T* method is defined as "speed by *T* method" and expressed as ω_t, and the speed obtained by the proposed method is defined as "estimated speed" and expressed as ω_e.

The experimental results of the orthogonal position signal, the Fourier analysis, the sampling position $\hat{\theta}_e$, the interpolation position θ_i, the estimated position θ_e, and the position errors $\Delta\hat{\theta}_e$ using the M method, $\Delta\theta_i$ using the least square interpolation method, and $\Delta\theta_e$ using the proposed detection method at 2.5 r/min are shown in Figs. 12–14, respectively. The harmonic content using different methods are shown in Table II. It can be seen from Fig. 12(a) that the discrete signal is obvious in

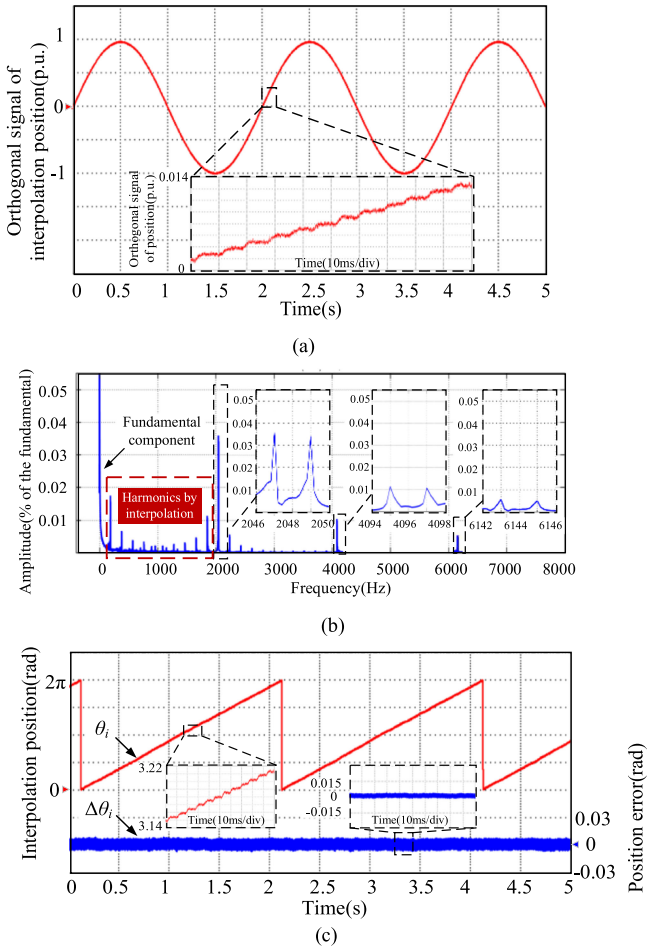

Fig. 13. Experimental results using the least-square interpolation method. (a) Discontinuous orthogonal position signal. (b) Fourier analysis of the orthogonal position signal. (c) Sampling position and position error.

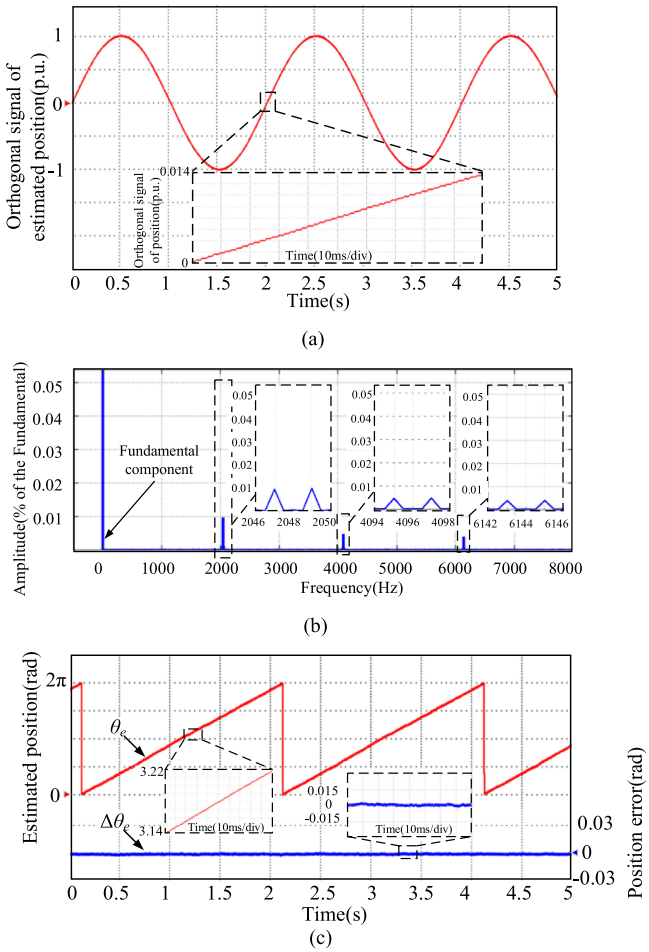

Fig. 14. Experimental results using the proposed method. (a) Discontinuous orthogonal position signal. (b) Fourier analysis of the orthogonal position signal. (c) Estimated position and position error.

TABLE II
HARMONIC CONTENT USING DIFFERENT METHODS

	k=1	k=2	k=3
M method	0.049%	0.025%	0.017%
	0.048%	0.024%	0.016%
Least-square interpolation method	0.037%	0.012%	0.005%
	0.036%	0.011%	0.004%
CDNF+PLL	0.010%	0.006%	0.005%
	0.009%	0.005%	0.004%

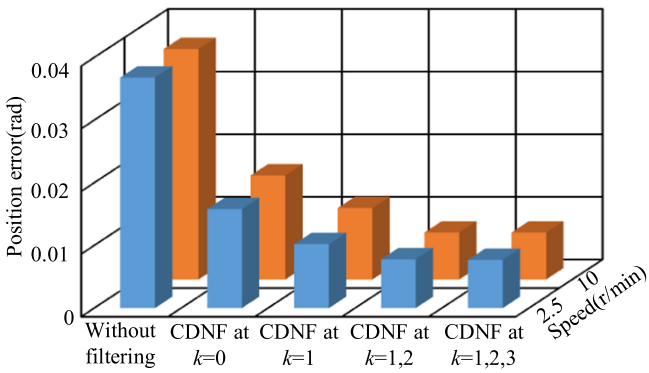

Fig. 15. Position errors in different k at 2.5 r/min and 10 r/min.

the orthogonal position signal. And the ($kN\pm1$)th harmonics can be observed in the Fourier spectrum from Fig. 12(b). The harmonic amplitudes can be decreased by using the least-square interpolation method. However, since the accuracy of interpolating is affected by the real-time operation state of the motor, inaccurate interpolation may occur, which can result in the additional harmonics. After the proposed detection method is adopted, the ($kN\pm1$)th harmonics are effectively suppressed. It can be seen that the proposed method can filter the harmonics of specific frequencies effectively.

The experimental results of sampling position and position error are shown in Fig. 12(c) at 2.5 r/min and rated load. It can be seen that the discrete position can be observed obviously, and there exists the position error whose amplitude is 0.03rad. The position error can be decreased by using the least-square interpolation method to 0.012rad as shown in Fig. 13(c). After using the proposed detection method in Fig. 14(c), the discrete position signal can be extracted effectively. The estimated position signal can fit the actual position, and the position error can be decreased to 0.002rad.

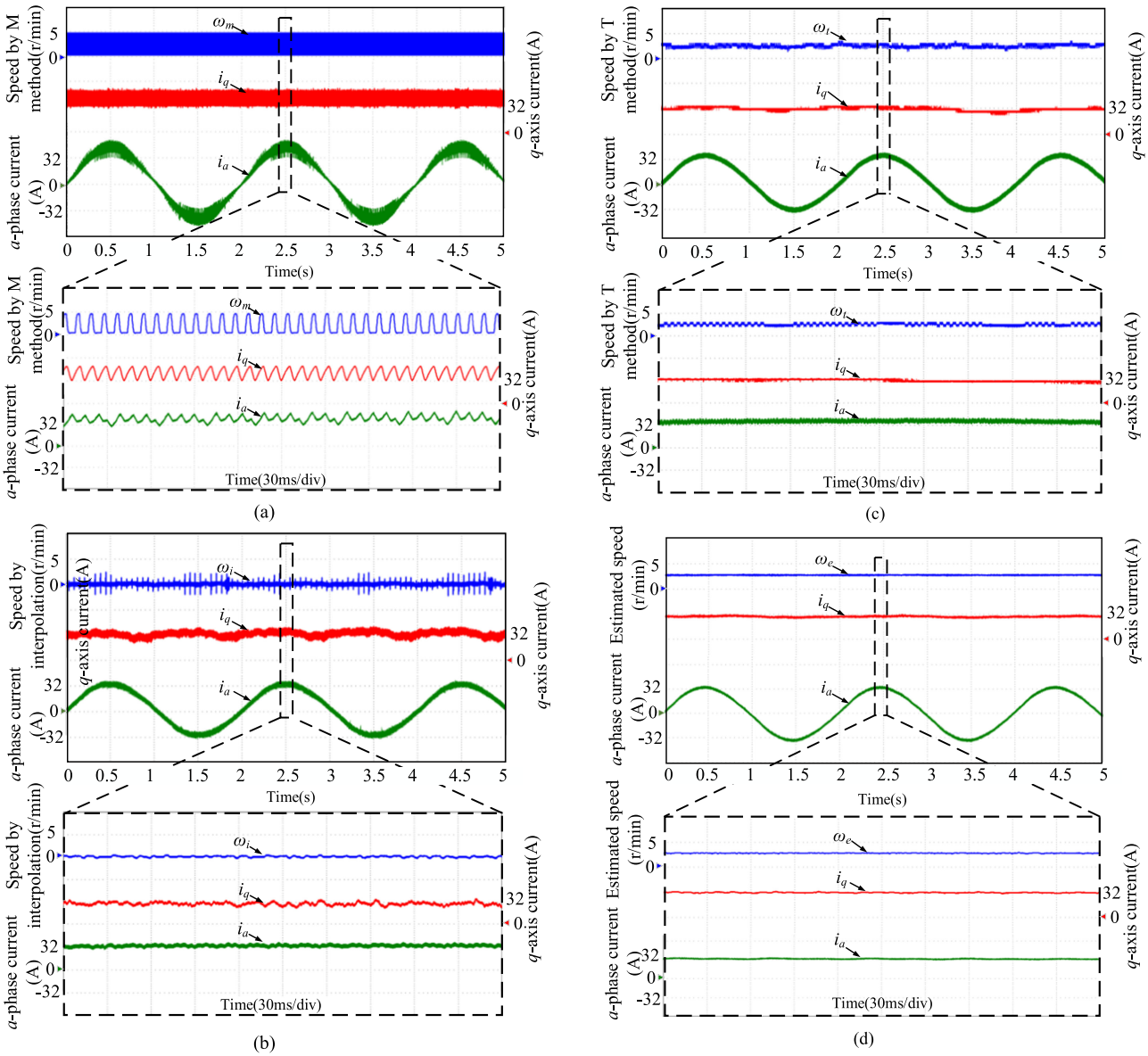

Fig. 16. Experimental comparison of the *M* method, the interpolation method, the *T* method, and the proposed estimated method at 2.5 r/min and rated load. (a) The *M* method. (b) The least-square interpolation method. (c) The *T* method. (d) The proposed method.

The position errors are shown in Fig. 15 in different k at 2.5 and 10 r/min, where CDNF at $k = 0$ is the complex filter. It can be seen that when $k = 1$ and $k = 12$, increasing the harmonic extraction modules can obtain better filtering effect, while it is not obvious when $k = 12$, 3 compared with $k = 12$. So, obvious filtering effect can be obtained by filtering the first two harmonics of $k = 1$ and 2 in practical applications.

The experimental comparison of the *M* method, the interpolation method, the *T* method, and the proposed estimated method at 2.5 r/min and rated load is shown in Fig. 16, which contains the speed, the *q*-axis current and the *a*-phase current. When using the sampling position and speed by *M* method as feedback, the speed by *M* method presents pulse fluctuations due to the low precision of the position, which reaches 5.1 r/min. The large fluctuations of speed feedback will be mainly superimposed on the *q*-axis current of the motor in Fig. 16(a) which reaches 21.3 A. The speed fluctuations can be decreased by using the least-square interpolation method to 1.9 r/min. However, since the accuracy of interpolation is affected by the real-time operation state of the motor, inaccurate interpolation may occur. Thus, there are still some fluctuations in the speed after the least-square interpolation. And the current ripple in the *q*-axis current is diminished from 21.3 to 7.84 A in Fig. 16(b). Using the *T* method can reduce the speed fluctuations to 1.2 r/min and the *q*-axis current fluctuation to 5.56 A in Fig. 16(c). After adopting the proposed method, the fluctuations in the *q*-axis current are diminished to 1.22 A. The speed fluctuations are restrained to 0.6 r/min in Fig. 16(d).

The experimental comparison of the *M* method, the interpolation method, and the proposed estimated method with speed variation from 2.5 to 50 r/min at 50% rated load is shown in Fig. 17. In each figure, the speed, the speed error, and position error are

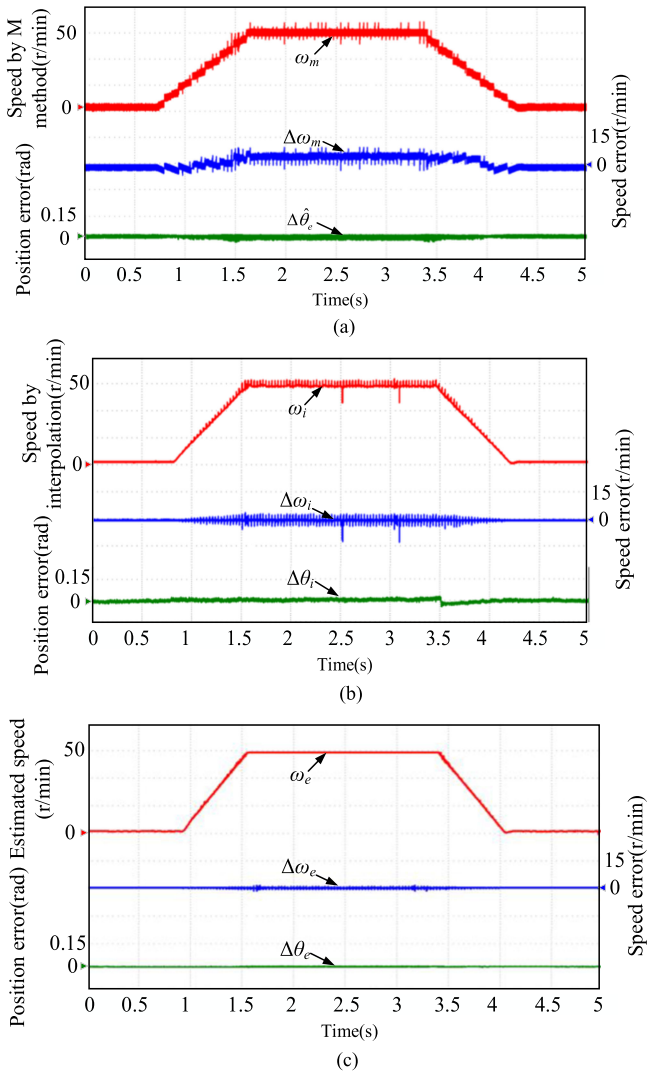

Fig. 17. Experimental comparison of the *M* method, the interpolation method, and the proposed estimated method with speed variation from 2.5 to 50 r/min. (a) The *M* method. (b) The least-square interpolation method. (c) The proposed method.

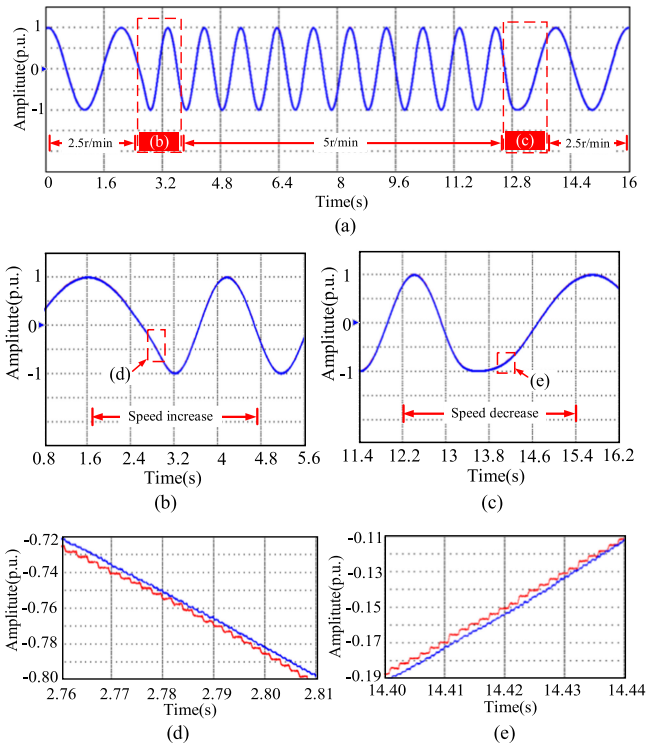

Fig. 18. Experimental results about the self-adaptability of CDNF. (a) Position orthogonal signal. (b) Position orthogonal signal at speed-rising process. (c) Position orthogonal signal at speed-dropping process. (d) Detail of (b). (e) Detail of (c).

given. It can be seen that there are fluctuations in the speed by *M* method whose error reaches 5.1 r/min, and the position error is 0.03 rad in Fig. 17(a). The speed fluctuations can be decreased by using the least-square interpolation method to 2.4 r/min and the position error to 0.011 rad shown in Fig. 17(b). After using the proposed method, the fluctuations of the estimated speed have been restrained effectively, which can be suppressed to 1.1 r/min. And the position error can be restrained to 0.002 rad shown in Fig. 17(c).

The experimental results about the self-adaptability of CDNF are shown in Fig. 18 with the change of the speed reference. The initial speed reference is set as 2.5 r/min then increased to 5 r/min at 10 s and decreased to 2.5 r/min at 25 s. It can be seen that when the speed changes, the position orthogonal signal after CDNF can track the discontinuous position orthogonal signal well, which can obtain the fundamental frequency signal required in the PLL.

The experimental comparison of the *M* method, the interpolation method, the *T* method, and the proposed estimated method with step load disturbance from 20% to 100% rated load at 0.5 r/min are shown in Fig. 19, which contains the speed, the speed error and the position error.

It can be observed that the fluctuations have been effectively suppressed with the proposed method. The speed error is 0.2 r/min and the position error is 0.003 rad using the *M* method in Fig. 19(a). The speed error can be decreased by using the least-square interpolation method to 0.09 r/min and the position error to 0.0011 rad as shown in Fig. 19(b). In Fig.19(c), at transient state in low-speed region using the *T* method, the long-time interval between two encoder pulses causes a large delay in the speed update. In addition, as the motor operates at near zero speed, the time interval between the first and the second encoder pulses is longer. Then, the inaccurate speed is calculated by the *T* method during this period. Thus, the speed by *T* method shows discontinuous at transient state at low speed. The speed error is reduced to 0.004 r/min and the position error to 0.0002 rad further with the proposed method in [see Fig. 19(d)].

The harmonic amplitude in the orthogonal position signals under different-resolution encoders are shown in Fig. 20. It can be seen that the harmonic amplitude content in the orthogonal position signal is relatively high using the *M* method, which can achieve 0.16%, 0.09%, and 0.04% in 512, 1024, and 2048P/R, respectively. And the amplitude increases with the decrease of the resolution of the encoder. The harmonics can be decreased to

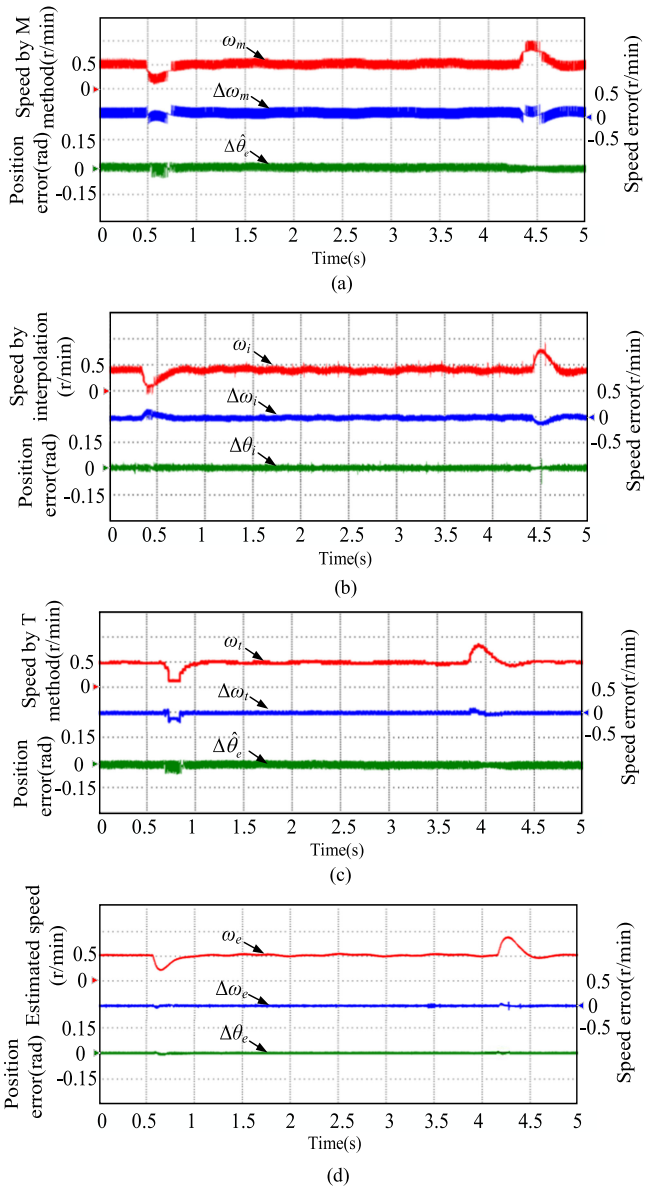

Fig. 19. Experimental comparison of the *M* method, the interpolation method, the *T* method, and the proposed estimated method with step load disturbance from 20% rated load to rated load at 0.5 r/min. (a)The *M* method. (b)The least-square interpolation method. (c) The *T* method. (d) The proposed method.

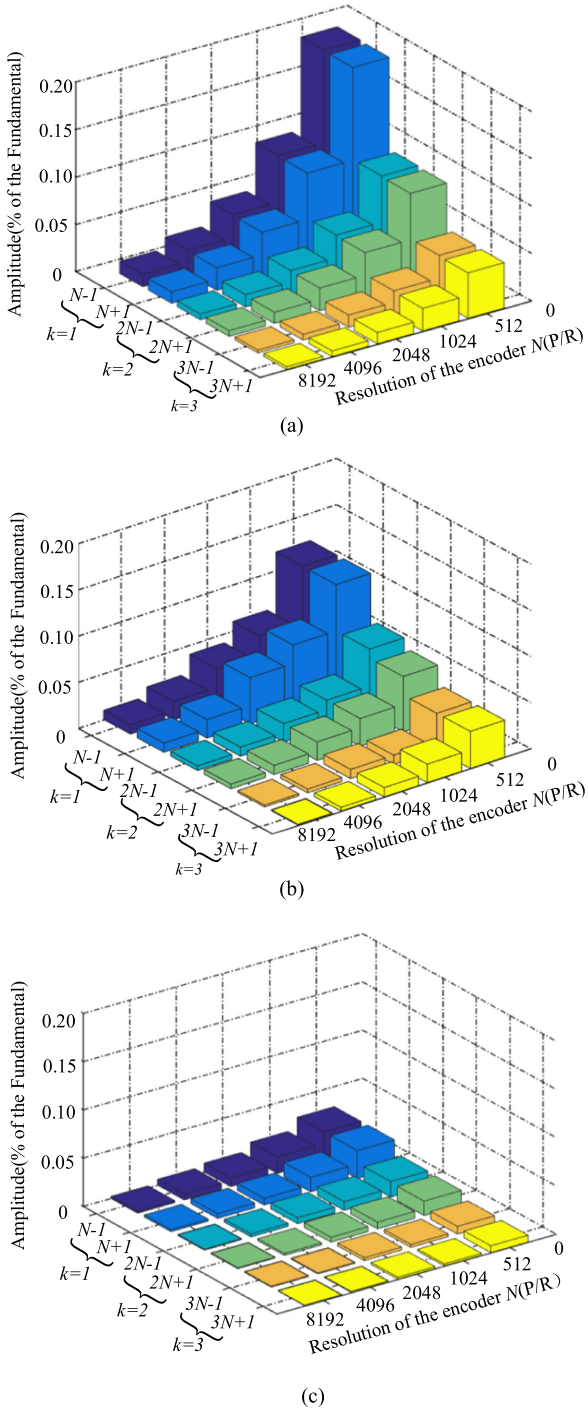

Fig. 20. Experimental results of the amplitude of harmonics in different resolutions. (a) The *M* method. (b) The least-square interpolation method. (c) The proposed method.

0.12%, 0.07%,, and 0.03% at 512, 1024, and 2048P/R, respectively by using the least-square interpolation method. When the proposed method is adopted, it can be noted that the harmonic amplitude of each frequency is effectively reduced to 0.03%, 0.02%, and 0.01% in 512, 1024, and 2048P/R, respectively. The estimation accuracy of position signal is improved effectively, and higher-precision position and speed are obtained.

The equivalent resolutions using CDNF with PLL at different speed references are shown in Fig. 21. It can be seen that the equivalent resolution of the encoders can be improved from 11b (2048P/R) to more than 13b (8192P/R), and the accuracy of the position has been improved effectively.

The actual speed and the position error when the motor running at one level and multiple levels is shown in Figs. 22 and 23, respectively, where one level is set as 2.8 m and the multiple levels are set as 36.5 m which are 13 levels. It can be concluded that the motion conditions of the traction motor can be divided into four stages: zero-servo stage, speed-increasing stage, constant speed stage, and speed-decreasing stage. At the beginning of the motion, the brake of the traction motor is open in order to obtain the initial rotor position. Then, the motor enters the speed-increasing stage until the speed arrives the speed

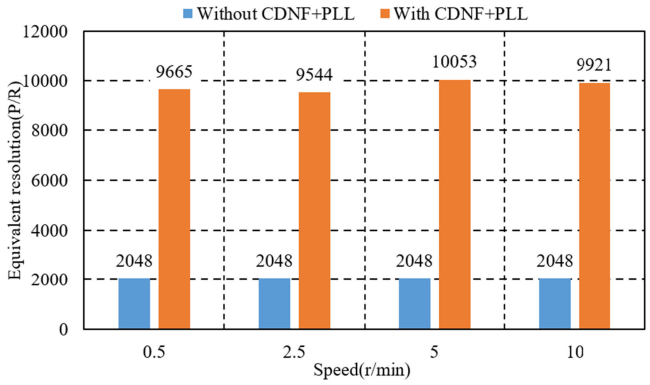

Fig. 21. Equivalent resolutions using CDNF with PLL at different speed references.

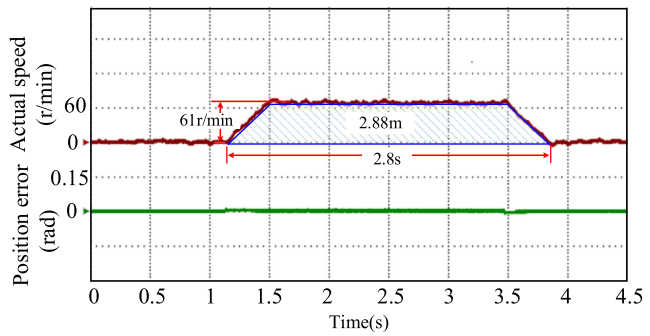

Fig. 22. Experimental results of actual speed, and position error when the elevator runs one level.

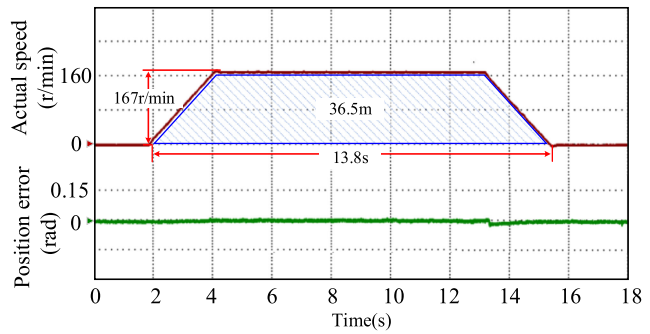

Fig. 23. Experimental results of actual speed, and position error when the elevator runs multiple levels.

reference. The speed reference of the elevator is determined by the operation distance. When the elevator passes through fewer levels, the speed reference is set as low operation speed of the elevator n. The multiple levels usually lead to the rated speed to set as the operation speed of the elevator in the constant speed stage. After reaching the set running time, the traction motor decelerates and stop running. The area between the motion track and the time axis is the running distance of the traction motor.

VI. Conclusion

This article proposed a position and speed detection method based on CDNF method combined with PLL for gearless traction motor drives using the ordinary-resolution encoder at low speed. The fundamental component can be obtained and the harmonics can be effectively filtered with this method. In this way, the continuous position orthogonal signal can be extracted, and then the position signal can be acquired by PLL. This method can automatically adjust the central frequency of the filter according to the change of the operating speed, and has valid effect for high-frequency harmonics. Based on the analysis of the parameters, a parameter design criterion is obtained with the maximum phase margin of the system. The experiment results show that the proposed position and speed detection method can obtain more accurate rotor position and speed at low-speed operation for gearless traction motor drives with ordinary-resolution encoders.

References

[1] X. Zhou, J. Sun, H. Li, and X. Song, "High performance three-phase PMSM open-phase fault-tolerant method based on reference frame transformation," *IEEE Trans. Ind. Electron.*, vol. 66, no. 10, pp. 7571–7580, Oct. 2019.

[2] G. Wang, R. Yang, and D. Xu, "DSP-Based control of sensorless IPMSM drives for wide-speed-range operation," *IEEE Trans. Ind. Electron.*, vol. 60, no. 2, pp. 720–727, Feb. 2013.

[3] G. Wang, R. Liu, N. Zhao, D. Ding, and D. Xu, "Enhanced linear ADRC strategy for HF pulse voltage signal injection-based sensorless IPMSM drives," *IEEE Trans. Power. Electron.*, vol. 34, no. 1, pp. 514–525, Jan. 2019.

[4] F. Toso, D. Da Rù, P. Alotto, and S. Bolognani, "A moving horizon estimator for the speed and rotor position of a sensorless PMSM drive," *IEEE Trans. Power. Electron.*, vol. 34, no. 1, pp. 580–587, Jan. 2019.

[5] Y. Wang, Y. Feng, X. Zhang, and J. Liang, "A new reaching law for antidisturbance sliding-mode control of PMSM speed regulation system," *IEEE Trans. Power. Electron.*, vol. 35, no. 4, pp. 4117–4126, Apr. 2020.

[6] D. Liang, J. Li, R. Qu, and W. Kong, "Adaptive second-order sliding-mode observer for PMSM sensorless control considering VSI nonlinearity," *IEEE Trans. Power. Electron.*, vol. 33, no. 10, pp. 8994–9004, Oct. 2018.

[7] Y. Wang, Y. Xu, and J. Zou, "Sliding-mode sensorless control of PMSM with inverter nonlinearity compensation," *IEEE Trans. Power. Electron.*, vol. 34, no. 10, pp. 10206–10220, Oct. 2019.

[8] D. Bao, X. Pan, Y. Wang, X. Wang, and K. Li, "Adaptive synchronous-frequency tracking-mode observer for the sensorless control of a surface PMSM," *IEEE Trans. Ind. Appl.*, vol. 54, no. 6, pp. 6460–6471, Nov./Dec. 2018.

[9] Q. Ni *et al.*, "A new position and speed detection scheme for position control of PMSM drives using low-resolution position sensors," *IEEE Trans. Ind. Appl.*, vol. 55, no. 4, pp. 3747–3758, Jul./Aug. 2019.

[10] H. Seol, J. Lim, D. Kang, J. S. Park, and J. Lee, "Optimal design strategy for improved operation of IPM BLDC motors with low-resolution hall sensors," *IEEE Trans. Ind. Electron.*, vol. 64, no. 12, pp. 9758–9766, Dec. 2017.

[11] V. Repecho, D. Biel, and A. Arias, "Fixed switching period discrete-time sliding mode current control of PMSM," *IEEE Trans. Ind. Electron.*, vol. 65, no. 3, pp. 2039–2048, Mar. 2018.

[12] C. Lian, F. Xiao, S. Gao, and J. Liu, "Load torque and moment of inertia identification for permanent magnet synchronous motor drives based on sliding mode observer," *IEEE Trans. Power. Electron.*, vol. 34, no. 6, pp. 5675–5683, Jun. 2019.

[13] C. Park, "Performance comparison between the normal-conducting magnet and the superconducting magnet in LSM for high-speed propulsion," *IEEE Trans. Magn.*, vol. 53, no. 11, pp. 1–6, Nov. 2017.

[14] F. J. Toledo, J. M. Blanes, and V. Galiano, "Two-step linear least-squares method for photovoltaic single-diode model parameters extraction," *IEEE Trans. Ind. Electron.*, vol. 65, no. 8, pp. 6301–6308, Aug. 2018.

[15] L. Ortombina, F. Tinazzi, and M. Zigliotto, "Magnetic modeling of synchronous reluctance and internal permanent magnet motors using radial basis function networks," *IEEE Trans. Ind. Electron.*, vol. 65, no. 2, pp. 1140–1148, Feb. 2018.

[16] A. Abbaszadeh, D. Arab Khaburi, and J. Rodríguez, "Predictive control of permanent magnet synchronous motor with non-sinusoidal flux distribution for torque ripple minimisation using the recursive least square identification method," *IET Elect. Power Appl.*, vol. 11, no. 5, pp. 847–856, 2017.

[17] Q. Jiang, X. Yan, H. Yi, and F. Gao, "Data-driven batch-end quality modeling and monitoring based on optimized sparse partial least squares," *IEEE Trans. Ind. Electron.*, vol. 67, no. 5, pp. 4098–4107, May 2020.
[18] M. Z. Ali, M. N. S. K. Shabbir, X. Liang, Y. Zhang, and T. Hu, "Machine learning-based fault diagnosis for single- and multi-faults in induction motors using measured stator currents and vibration signals," *IEEE Trans. Ind. Appl.*, vol. 55, no. 3, pp. 2378–2391, May/Jun. 2019.
[19] J. Zhao, J. Zhao, H. Wang, J. Song, and F. Dong, "Precision position measurement of linear motors mover based on temporal image correlation," *IEEE Trans. Instrum. Meas.*, vol. 68, no. 9, pp. 3268–3277, Sep. 2019.
[20] Y. Miao, H. Ge, M. Preindl, J. Ye, B. Cheng, and A. Emadi, "MTPA fitting and torque detection technique based on a new flux-linkage model for interior-permanent-magnet synchronous machines," *IEEE Trans. Ind. Appl.*, vol. 53, no. 6, pp. 5451–5460, Nov./Dec. 2017.
[21] X. Wu, S. Huang, K. Liu, Y. Hu, W. Pan, and X. Peng, "Enhanced position sensorless control using bilinear recursive least squares adaptive filter for interior permanent magnet synchronous motor," *IEEE Trans. Power. Electron.*, vol. 35, no. 1, pp. 681–698, Jan. 2020.
[22] Q. An, J. Zhang, Q. An, and A. Shamekov, "Quasi-proportional-resonant controller based adaptive position observer for sensorless control of PMSM drives under low carrier ratio," *IEEE Trans. Ind. Electron.*, vol. 67, no. 4, pp. 2564–2573, Apr. 2020.
[23] J. Kim, S. Choi, K. Cho, and K. Nam, "Position estimation using linear hall sensors for permanent magnet linear motor systems," *IEEE Trans. Ind. Electron.*, vol. 63, no. 12, pp. 7644–7652, Dec. 2016.
[24] X. Song, B. Han, S. Zheng, and J. Fang, "High-precision sensorless drive for high-speed BLDC motors based on the virtual third harmonic back-EMF," *IEEE Trans. Power. Electron.*, vol. 33, no. 2, pp. 1528–1540, Feb. 2018.
[25] J. Cai, Z. Liu, Y. Zeng, H. Jia, and Z. Deng, "A hybrid-harmonic-filter-based position estimation method for an SRM with embedded inductive sensing coils," *IEEE Trans. Power. Electron.*, vol. 33, no. 12, pp. 10602–10610, Dec. 2018.
[26] S. Carpiuc, "Rotor temperature detection in permanent magnet synchronous machine-based automotive electric traction drives," *IEEE Trans. Power. Electron.*, vol. 32, no. 3, pp. 2090–2097, Mar. 2017.
[27] L. Dong, Y. Huang, J. Jatskevich, and J. Liu, "Improved fault-tolerant control for brushless permanent magnet motor drives with defective hall sensors," *IEEE Trans. Energy Convers.*, vol. 31, no. 2, pp. 789–799, Jun. 2016.

Yin Bai received the B.S. and M.S degrees in electrical engineering, in 2017 and 2019, respectively, from Harbin institute of technology, Harbin, China, where he is currently working toward the Ph.D degree in PMSM drives control with Harbin institute of technology, China.

His current research interests include advanced control of permanent magnet synchronous motor drives at low-speed operation.

Gaolin Wang (Senior Member, IEEE) received the B.S., M.S., and Ph.D. degrees in electrical engineering from Harbin Institute of Technology, Harbin, China, in 2002, 2004, and 2008, respectively.

In 2009, he joined the Department of Electrical Engineering, Harbin Institute of Technology as a Lecturer, where he has been a Full Professor of electrical engineering since 2014. From 2009 to 2012, he was a Postdoctoral Fellow with Shanghai Step Electric Corporation, where he was involved in the traction machine control for direct-drive elevators. He has authored more than 100 technical papers published in journals and conference proceedings. He is the holder of ten Chinese patents. His current major research interests include permanent magnet synchronous motor drives, high performance direct-drive for traction system, position sensorless control of ac motors, efficiency optimization control of PMSM, and digital control of power converters.

Dr. Wang serves as a Guest Associate Editor for the IEEE TRANSACTIONS ON INDUSTRIAL ELECTRONICS, an Associate Editor for the IEEE ACCESS, *IET Electric Power Applications*, and *Journal of Power Electronics*.

Guoqiang Zhang (Member, IEEE) received the B.S. degree in electrical engineering from Harbin Engineering University, Harbin, China, in 2011, and the M.S. and Ph.D. degrees in electrical engineering from Harbin Institute of Technology, Harbin, China, in 2013 and 2017, respectively.

Since 2017, he has been with the Department of Electrical Engineering, Harbin Institute of Technology, where he is currently an Associate Professor. His current research interests include control of electrical drives, and parameter identification technique, with main focus on sensorless field-oriented control of synchronous motor drives.

Dr. Zhang serves as an Associate Editor for *Journal of Power Electronics*.

Nannan Zhao (Member, IEEE) received the B.S. and M.S. degrees in control science and engineering, and the Ph.D. degree in electrical engineering, all from Harbin Institute of Technology, Harbin, China, in 2013, 2015, and 2019, respectively.

He is currently a Postdoctoral Fellow and a Lecturer with the School of Electrical Engineering and Automation, Harbin Institute of Technology. His current research interests include advanced control of permanent magnet synchronous motor drives and position sensor-less control of ac motors.

He is currently supported by Postdoctoral Innovative Talent Support Program of China.

Dianguo Xu (Fellow, IEEE) received the B.S. degree in control engineering from Harbin Engineering University, Harbin, China, in 1982, and the M.S. and Ph.D. degrees in electrical engineering from Harbin Institute of Technology (HIT), Harbin, China, in 1984 and 1989, respectively.

In 1984, he joined the Department of Electrical Engineering, HIT as an Assistant Professor. Since 1994, he has been a Professor with the Department of Electrical Engineering, HIT. From 2000 to 2010, he was the Dean of School of Electrical Engineering and Automation, HIT, where he is currently the Vice President. His research interests include renewable energy generation technology, power quality mitigation, sensorless vector controlled motor drives, high performance servo system. He has authored or coauthored more than 600 technical papers.

Dr. Xu is a fellow of IEEE, Chairman of IEEE Harbin Section, Co-EIC of IEEE TRANSACTIONS ON POWER ELECTRONICS, Associate Editor of the IEEE TRANSACTIONS ON INDUSTRIAL ELECTRONICS, IEEE Journal of Emerging and Selected Topics in Power Electronics. He received the 2018 IEEE IAS Outstanding Achievement Award.